Joint inversion of GPS and high-resolution GRACE gravity data for the 2012 Wharton basin earthquakes

Michel Diament, Valentin Mikhailov, Elena Timoshkina

To cite this version:

Michel Diament, Valentin Mikhailov, Elena Timoshkina. Joint inversion of GPS and high-resolution GRACE gravity data for the 2012 Wharton basin earthquakes. Journal of Geodynamics, 2020, 136, pp.101722 -. 10.1016/j.jog.2020.101722 . hal-03489750

HAL Id: hal-03489750
https://hal.science/hal-03489750v1

Joint inversion of GPS and high-resolution GRACE gravity data for the 2012 Wharton basin earthquakes

Michel Diament[1], Valentin Mikhailov[2], Elena Timoshkina[2]

[1] Université de Paris, Institut de physique du globe de Paris, CNRS, IGN, F-75005 Paris, France

[2] Schmidt Institute of Physics of the Earth, Russian Academy of Sciences, 10 B. Gruzinskaya, Moscow, 123995 Russia

Abstract

The Wharton basin is situated in the north-eastern part of the Indian Ocean. In 2012 it hosted the largest intraplate strike-slip earthquakes ever recorded by geophysical networks. The M_w 8.6 earthquake of April 11, 2012, was preceded by a major foreshock (M_w 7.2) on January 10 and was followed two hours afterward by a M_w 8.2 event. These three large events occurred at the diffuse boundary between the Indian and Australian plates and were almost pure strike-slips on sub-vertical rupture surfaces. Using GRACE data, we first extracted the coseismic and postseismic gravity signals caused by these earthquakes. Then we fitted both GPS and the highest available spatial resolution of GRACE data using the geometry of the fault system suggested by Hill et al. (2015). We propose a regularization, which allows to solve for a linear problem in order to invert GPS and GRACE data under constraints on the rake angle. Our inversion yields a uniform displacement field on all elements of a given fault plane. Our solution shows that even the main displacement occurred on WNW trending faults, comparable displacement also occurred on a rupture striking NNE. Hence, we show that the deformation in this diffuse plate boundary region in 2012 was accommodated by displacements along both fault-systems.

A viscoelastic relaxation of the asthenosphere with a Maxwell viscosity 10^{19} Pa·s successfully explains the postseismic displacements at GPS sites and postseismic gravity signals. The limited postseismic aftershock activity suggests small postseismic slip in the area of the 2012 Wharton earthquakes contrary to what is often observed after large subduction event. Because a part of the observed signal could be related to afterslip, our obtained Maxwell viscosity value should be considered as a lower limit of the asthenospheric viscosity below the Wharton basin.

Keywords: Wharton basin, Indian Ocean, 2012 earthquake, GRACE gravity, GPS, joint inversion, asthenospheric viscosity

Introduction

Located in the north-eastern part of the Indian Ocean, to the East of the Ninety East Ridge (NER), the Wharton basin in 2012 hosted the largest intraplate strike-slip earthquakes ever recorded by geophysical networks. The M_w 8.6 earthquake of April 11, 2012 with a hypocentre at a depth d=20 km (NEIC catalogue of the USGS), was preceded by a major foreshock (M_w 7.2, d=19 km) on January 10 and was followed two hours afterward by a M_w 8.2 event, d=25 km (Fig.1). These three large events were almost pure strike-slips on sub-vertical rupture surfaces (e.g., Duputel et al., 2012; Satriano et al., 2012; Meng et al., 2012; Yue et al., 2012; Ishii et al., 2013; Wei et al., 2013; Hill et al., 2015).

These seismic events occurred southward of the area struck by the megathrust Sumatra-Andaman (26 December 2004, M_w 9.2) and Nias (28 March 2005, M_w8.6) events in a region classified as a diffuse boundary between the Indian and Australian plates, that is supposed to accommodate about 11 mm/year of relative motion (e.g., DeMets et al., 2010).

The origin of this diffuse boundary is still debated. Space geodetic data from sites within Australia and Indian plates support the existence of distinct Indian, Capricorn, and Australian plates separated by diffuse oceanic plate boundaries (Gordon et al., 2008 and references herein). Reanalysing satellite-derived gravity anomalies and marine magnetic anomalies Jacob et al. (2014) proposed a new tectonic scenario for the study area. The “hard collision” between Indian and Eurasian plates ~40Ma led to a ~50° clockwise change of the spreading direction between India and Antarctica (Patriat and Achache, 1984). Seafloor spreading along the Wharton ridge ceased consequently, as shown by the presence of a fossil spreading centre in the Wharton Basin (Liu et al., 1983). Since that time, the Indian and Australian plates have been moving in parallel, but because of the resistance due to the collision of India with Eurasia, the Indian plate is moving northward ∼11 mm/year slower than the Australian plate. The broad diffuse zone including a system of transform faults within the Wharton basin accommodates this difference. Jacob et al. (2014) model predicts a total compression of ~180 km across this diffuse boundary.

Figure 1

Earthquakes in the Wharton basin are generally occurring predominantly along preexisting and reactivated NNE trending strike-slip faults (Deplus et al., 1998; Abercrombie et al., 2003; Rajendran et al., 2011; Aderhold & Abercrombie, 2016). However, the seismic rupture of the 2012 Wharton events appeared to be more complex. The CMT solution for the main shock provided two fault planes with strike, dip, slip $\{20^{\circ}, 76^{0}, 5^{0}\}$ and $\{289^{\circ}, 85^{0}, 166^{0}\}$ (http://www.globalcmt.org/CMTsearch.html). The 20° plane coincides with NNE system of left-lateral reactivated faults clearly seen on seismic profiles and bathymetry (e.g. Deplus et al., 1998). However, seismological results, including backprojection (Meng et al., 2012; Yue et al., 2012; Ishii et al., 2013), W phase inversion (Duputel et al., 2012), joint inversion of regional and teleseismic waveform data (Yue et al., 2012; Wei et al., 2013), aftershock locations, as well as finite fault models based on GPS data (Hill et al., 2015) revealed that the rupture reactivated an orthogonal system of NNE left-lateral and WNW right-lateral faults. The NNE strike-slip faults are deep structural boundaries formed at the Wharton spreading centre during the Eocene (e.g. Jacob et al., 2014). On the contrary, the WNW faults are likely to be much younger (e.g. Carton et al., 2014) and some models predict that the main shortening is mostly accommodated on the WNW trending faults (Duputel et al., 2012, Yue et al., 2012; Ishii et al., 2013).

Until recently no WNW active structures were found in the basement topography or seismic profiles (Geersen et al., 2015). But analysing new seismic profiles, Carton et al. (2014) and Qin and Singh (2015) found inclined reflectors extending into the mantle down to 35-37 km and dipping at 30-45 degree. Singh et al. (2017) reported a system of conjugate faults in the area of the M_w 8.2 aftershock.

Zang et al. (2012) backprojected teleseismic P wave observed at three distant regional seismic networks. Their results indicate that the earthquake ruptured a conjugate fault system, composed of two subparallel WNW-ESE faults, and a NNE-SSW fault. They did not invoke displacement along the Ninety East Ridge as reported in other studies.

Another interesting feature of these earthquakes is that they ruptured the upper mantle. Indeed, estimated centroid depth is about 30 km (Duputel et al., 2012) and waveform inversions showed that rupture penetrated down to 50 or even 60 km deep (Yue et al., 2012, Wei et al., 2013). The results of a joint inversion of static GPS offsets and high-rate GPS data (Hill et al., 2015) support this conclusion. Even if it is well known that the mantle contributes most the strength of the oceanic lithosphere (e.g. Burov, 2011) such depth seems to contradict the results of laboratory studies (e.g. Boettcher et al., 2007), which predict that the transition from stable to unstable sliding occurs at about 600°C. According to Hill et al. (2015) this isotherm in the Wharton basin is at 30 km depth (we will discuss this point in more detail hereafter).

Because of the remote offshore location of the events, the GPS constraints on the fault geometry are limited. For example, Meng et al. (2012) concluded that only seismological data could be used to invert for the focal mechanisms. Hence, satellite GRACE gravity data might provide additional constraints on the coseismic deformation (e.g. Mikhailov et al., 2004). Studies of the Wharton events using GRACE data were performed by Han et al. (2015) and Dai et al. (2016). Analysing the low resolution GRACE models of the Center for Space Research (CSR), Houston, USA with N=40 spherical harmonics, Han et al. (2015) showed that the gravity changes were predominantly produced by coseismic compression and dilatation within the oceanic crust and upper mantle and by postseismic viscoelastic relaxation. Dai et al. (2016) analysed the temporal variations of the northern component of gravity and gravity gradient from CSR RL05 models up to degree 40 to study the coseismic signal.

Here we reinvestigate these earthquakes using more detailed gravity models from CSR and GRGS (Groupe de Recherche de Géodésie Spatiale, France) centres computed up to degree 96 and 80 spherical harmonics respectively. Below, we first discuss the extraction of coseismic and postseismic signals, then we address the comparison of real and synthetic data and present our joint GPS – GRACE modelling of the co- and postseismic processes and discuss our results. Finally, we investigate the mantle viscoelastic postseismic response and estimate the Maxwell viscosity of the asthenosphere.

1. Extraction of coseismic and postseismic signal from the GRACE data

Several centres deliver time-series of the GRACE gravity models. Among them are CNES/GRGS in Toulouse, France; GFZ in Potsdam, Germany; CSR in Austin, USA; JPL in Pasadena, USA; AIUB in Bern, Switzerland; TU in Graz, Austria; TONGJI in Shanghai and HUST in Wuhan, China. CNES/GRGS solutions are supposed to be ready for use and do not need any additional filtering (Lemoine et al., 2013). For all other centres, unfiltered and filtered by a dedicated DDK filter solutions are available. To regularize the normal equation, the DDK filter (Kusche, 2007, Kusche et al., 2009) uses a priori error covariance matrices derived from GRACE processing. Depending on the level of filtering, a set of GRACE CSR models is available, from more smoothed DDK1 to less smoothed DDK8 or even unfiltered. From this large set of models we analysed the most widely used not smoothed CSR solutions up to spherical harmonics (SH) degree N=40; moderately smoothed (DDK5) CSR solutions up to the maximum available number of SH $N=96$; CNES/GRGS ones with N=50 and N=80. This choice covers a wide range of existing models.

To extract the coseismic and postseismic signals in the Wharton basin we fitted the gravity time-series $V_z(\lambda,\phi,t)$ in every point (λ,ϕ) with two linear trends in the mean squared sense:

$$V_z(\lambda,\phi,t) = \begin{cases} a_1(\lambda,\phi) + b_1(\lambda,\phi)(t - t_0) & t < t_e \\ a_2(\lambda,\phi) + b_2(\lambda,\phi)(t - t_0) & t > t_e \end{cases} \qquad (1)$$

where λ is the latitude, φ is the longitude, t_0 is the date of the first gravity model used in our calculations, t_e is the date of the considered seismic event, a_1, b_1 and $, a_2, b_2$ are parameters of the linear trends before and after the seismic event.

The coseismic jump in the gravity time series is estimated as:

$$\delta(\lambda,\phi) = a_2(\lambda,\phi) + b_2(\lambda,\phi)(t_e - t_0) - a_1(\lambda,\phi) - b_1(\lambda,\phi)(t_e - t_0), \qquad (2)$$

and the coseismic jump plus the postseismic trend as:

$$a_2(\lambda,\phi) + b_2(\lambda,\phi)(t_f - t_0) - a_1(\lambda,\phi) - b_1(\lambda,\phi)(t_f - t_0), \qquad (3)$$

where t_f stands for the date of the last gravity model used in calculations.

In the presence of a high level of noise, the estimation of the coseismic and postseismic signals by equations (2-3) appears to be an unstable problem. Therefore, to confirm the estimated coseismic signal given by equation 2 we also used the difference of average values before and after the earthquake as suggested by Han et al. (2015):

$$\sum_{i=1}^{k-1} V_z(\lambda,\phi,t_i) - \sum_{i=k+1}^{N} V_z(\lambda,\phi,t_i), \qquad (4)$$

Here, the date of model k coincides with the month of the earthquake. Since we averaged over several months after the event, the extracted jump also includes some part of the postseismic gravity signal.

Figure 2 shows the coseismic jumps we obtained applying our different approaches to solutions from different processing centres with different spatial resolution starting from January 2008 up to April 2012 and adding annual and semi-annual components. The coseismic jump on plots A-C is calculated applying equation 4 to unfiltered CSR model truncated at N=40 (A), DDK-5 filtered CSR model up to N=*96* (B), and GRGS N=80 models (C). Plot D shows the coseismic jump estimated as the difference of two linear trends (equation. 2) using DDK-5 filtered CSR N=96 model. Plot E shows the coseismic plus postseismic signals calculated using equation 3 and the same CSR N=96 model as on plot (D).

Comparison of plots A to E shows that the location of all extrema is almost identical. Indeed, the half-wavelength of the shortest harmonic corresponding to N=40 is $\mathrm{l} = \pi \mathrm{R_{earth}}/\mathrm{N} \approx 500\ km$ ≈5° whereas for N=96 l is about 209 km. Hence, for N=40 the uncertainty in the position of a maximum or minimum value is about 250 km and for N=96 it is about 105 km. It is worth noting that the shift of the extrema for the high resolution signals (N=96 on plots B and N=80 on plot C) is relatively small when comparing with the low resolution model (plot A). This results from the filtering of the higher harmonics in CSR and GRGS solutions, which significantly reduces the upper part of their spectra. One should take this into account when comparing observed and computed signals. The morphology of the anomalies shown on plots B to D on Figure 2 is very close. The amplitude of signals on plots B and C is higher than on plot D, because using equation 4, we add a part of the postseismic signal to the coseismic one.

Figure 2

Figure 3 shows the gravity time-series in the centres of the negative lobes for CSR and GRGS models with different number of SH. Not-smoothed CSR N=40 models are rather noisy (Fig 3A) so only the more stable jump from average values (equation 4) can be extracted. Considering extracted trends and jumps as a signal and the difference between the real series and the signal as a noise, we found that the noise level is everywhere approximately the same, but of cause the signal-to-noise ratio is much higher in the points of extrema. Estimates of the co- and postseismic signals appear more reliable for higher resolution models. Therefore, we decided to use CSR N=96 models. We estimated the coseismic gravity jump (figure 2 D) as a difference of two trends (equation 2), and used equation 3 to extract the total coseismic plus postseismic signal (Figure 2E) removing annual and semi-annual components.

Figure 3

2. Comparison of synthetic and real data

When comparing a synthetic signal to the observed one, it is desirable to filter the synthetic signal with the same filter used for processing the real one. For the GRACE data this becomes critical when *N*>50. Filtering applied by different agencies is adaptive, e.g. DDK filter uses an a priori error covariance matrices derived from GRACE raw data processing. Because it is impossible to reproduce the thorough processing developed by the different groups producing GRACE models, we suggest to apply a filtering calibrated upon a well-known signal from another large earthquake. We used a roll-off filter proposed by F. Pollitz in his Static1D package (https://earthquake.usgs.gov/research/software/ #STATIC1D) applied to the spherical harmonics higher than $l > \frac{L_{max}}{2}$,:

$$F(l) = 1 - cos\left(\pi\left(1 - \frac{l}{L_{max}}\right)\right), \qquad (5)$$

where L_{max} is the number of SH in the synthetic model.

We calibrated the filter (5) using the rupture model of the 2004 Sumatra earthquake determined with a high accuracy from seismology, geodesy and tide gauge data by Lorito et al. (2010). We used their set of rectangular elements and GPS data and added the coseismic GRACE gravity signal. We determined the coseismic along-strike and along-dip displacements by minimizing a functional composed of: (1) the RMS residual of the calculated and measured northwards and eastwards displacements at GPS sites, normalized to the square of the maximum displacement and, (2) the RMS of the real minus synthetic gravity signal, normalized to the maximum value of the gravity signal and taken with a weight factor < 1. To calculate the displacements and the associated gravity signal, we used the Static 1D code developed by F. Pollitz, which solves the problem of a rectangular dislocation in a spherically stratified self-gravitating planet (Pollitz, 1996).

The best fit of synthetic to observed GPS displacements and GRGS gravity signals is obtained when calculating synthetic models up to L_{max} = 100 (Mikhailov et al., 2018). Hence, to mimic the processing used in the GRGS solution, the synthetic field should be calculated up to a larger number of SH than there is in the GRACE gravity models (in our case, up to *N*=100 for the GRGS models containing 80 SH). For the more noisy CSR data containing 96 SH, the best result was obtained applying a simple truncation of SH at *N*=80.

3. Comparison with fault plane models based on GPS displacements and seismic waveforms.

Different fault-plane models were proposed for the 2012 Wharton seismic events. They mostly differ by the length and strike of the faults (see Singh et al., 2017). To jointly invert GPS and GRACE data, we used the fault-plane model proposed by Hill et al. (2015), based on a joint inversion of high-rate GPS data, teleseismic observations, source time functions from broadband surface waves, and far-field static GPS displacements. The GPS sites in the nearest zone belong to the SuGAr network, which consists of GPS stations situated along the Sumatra subduction zone (Figure 4). The SuGAr network is operated and maintained by the Indonesian Institute of Sciences (LIPI) and the Earth Observatory of Singapore (EOS). In this study we used Static GPS offsets from 43 daily GPS solutions of the SuGAr network listed in the dataset S1 of Supplementary to Hill et al. (2015) adding station CBAY on the Nicobar Islands and stations HBAY, PORT, HAVE, MBDR on the Andaman Islands (Table 1 in Yadav et al., 2013,). Static GPS offsets were estimated using 10 days of data before and after the 11 April 2012 earthquakes, hence the offsets include effects of both the coseismic and early postseismic deformations. The real northing and easting GPS time series were fitted by two trends and a jump to get the offsets. We used the mean square error of the fits as a weight of every GPS station.

Our approach consists in minimizing a functional composed of the misfits of the weighted GPS northing and easting displacements, the weighted misfit of the gravity coseismic jumps and the weighted regularization condition, aimed to keep the rake close to an assigned direction. The minimization of the misfits in GPS and gravity in a mean-squared sense is a linear problem. However, adding the condition that the rake is close to a given value makes the functional nonlinear because the tangent of the rake angle is the ratio of the dip-slip D to the strike-slip S displacements on every element of a considered fault plane. To maintain linearity, we used the following approach. Let us consider a rupture model containing N planes, each plane being subdivided into K_i elements and with a rake angle at plane i being r_i, $i=1,2..N$. We use the following regularization condition:

$$\alpha \sum_{i=1}^{N} \left\{ \sum_{j=1}^{K_i} \left[\left(D_j\, cos(r_i) - S_j sin(r_i) \right)^2 + \left(D_j - \bar{D}_i \right)^2 + \left(S_j - \bar{S}_i \right)^2 \right] \right\} \qquad (6)$$

The first term in squared brackets requires the motions at plane i to occur along a direction with an azimuth r_i. Unfortunately, two vectors satisfy this condition: $\{D_j, S_j\}$ with the azimuth r_i and $\{-D_j, -S_j\}$ with the azimuth $r_i+180°$. The last direction is geodynamically meaningless and to exclude it we introduce two supplementary conditions in (6): the dip-slip (D_j) and strike-slip (S_j) displacements at every element of plane i are close to their average value over all plane i.

Our fault plane model includes four planes - marked I – IV on figure 4A - that we subdivide into different number of elements (see below). Numerical tests proved that the condition (6) effectively keeps displacements close to r_i and eliminates displacements in the opposite direction. The goodness of fit between the observed and synthetic GPS data depends on α, the relative weight of the condition (6). For the examples shown on figure 4, we iteratively found α assuming almost pure strike-slip at all planes keeping the maximum misfit at GPS sites smaller than 8%.

We first only inverted the GPS data using the Hill et al. (2015) fault-planes geometry and found that a good fit of the 48 GPS sites was achieved with almost pure strike-slip displacements on the four considered planes (Fig. 4). Figure 4B shows a solution when planes I-IV were subdivided along strike in 3, 3, 2 and 2 elements respectively, thus totally 10 elements and therefore 20 unknown values of D and S. Fig. 4A shows a solution for a more complex model in which the planes were subdivided along strike and dip into 3x3, 3x3, 2x2, and 2x2 elements respectively (26 elements and 52 unknowns).

For both cases, the computed displacements at GPS sites are very close to the observed ones (on Fig 4a, the synthetic arrows are above the real ones, on Fig.4b observed arrows are above). The displacement field on every plane is almost homogeneous. In the simplest model (10 elements), the displacement is on average 7.3 m on plane I, 4.8 m on plane II, 17.4 m on plane III and 3.6 m on plane IV. The difference between displacements on elements within each plane is in centimetres (Table 1). For the more detailed model, the displacements vary between 7.24 and 7.28 m, 4.77 and 4.81 m, 17.34 and 17.41 m, and 3.56 and 3.57 m for planes I-IV respectively. Thus, as already noted by Hill et al. (2015) the main displacement occurred on plane III striking WNW. A significant displacement also occurred on plane I striking NNE. Figure 4b shows that the low-resolution (N=40) gravity signal corresponding to the rupture model based on GPS data only, also fits well the observed one. This confirms Han et al. (2015) results. However, the observed and synthetic gravity signals significantly differ when taking into account a higher number of spherical harmonics (Fig. 4a). The synthetic gravity signal has larger amplitude than the observed ones. Indeed, the difference between the maximum values of the SE and NW observed and synthetic signals is 2.1 and 1 μGal, and reaches 3.7 μGal for the SW one. To improve the fit to the observed gravity data, we then performed a joint inversion for GPS and high resolution CSR satellite gravity data.

Figure 4

Figure5 shows the solution which fits both the GPS and GRACE CSR N=96 data under condition (6) on the rake angle. We assigned a weight of the GPS misfit 5 times bigger than that of the GRACE misfit and 2 times bigger than the weight of the condition (6) on the rake angle. The fit is good for both data sets (Table 1). For the GPS data the maximum misfit is 7.0%. The positive observed and synthetic SW and NE gravity lobes are now superimposed, and the maximum difference between the observed and synthetic signals is 1.4 μGal. We however note a shift of the SE and NW negative lobes of about 1^{o} in latitude and longitude. This shift is most probably caused by the DDK5 filtering of the highest harmonics. Figure 2 shows that depending on the applied filtering, on the number of harmonics and on the method of trend extraction, the position of extremum values is varying up to $1\text{-}2^{0}$.

Figure 5

The solution we obtain is again almost pure strike-slip. The displacements on fault planes I-IV are on average 7.0 m, 7.6 m, 12.2 m, and 0.3 m respectively with a difference of several cm between elements composing each plane (Table 1). In comparison to the inversion without gravity, the displacements on planes II increased by 2.8 m, and decreased on planes I, III and IV by 0.26 m, 5.2 m and 3.3 m. Displacement on the plane IV, situated at the Ninety East Ridge, became negligible (30 cm). This difference is not surprising since plane IV is the more distant from the GPS sites and therefore satellite gravity is better suited to estimate the displacement on this plane.

4 Discussion

The joint inversion of different geophysical data based on geodynamic models is now widely used (e.g. Tiberi et al., 2003; Basuyau et al., 2013). The advantage is that various independent data (GPS, seismic waveforms, CMT solutions, gravity anomalies etc.) can be inverted simultaneously or sequentially to get a set of model parameters (in our case, parameters of the fault planes, module and rake of displacement vectors) fitting all data. However, any geodynamic model is an approximation of the natural process under study. For instance, in our case, the numerical solution for a rupture within a spherically layered planet - which is commonly used for fault-plane inversion - does not account for the lateral variations of the lithospheric thickness and its composition, or of the presence of a subducting slab and numerous faults. Therefore, it is necessary to keep a balance between the precision and resolution of data, the accuracy of the natural process description through the numerical models used in an inversion on the one hand and the number of details and parameters, which one desires to explore through the inversion on the other hand. Our preferred model contains 26 elements, but with 10 elements it is possible to fit both the gravity and GPS observations with a reasonable accuracy.

In addition to a description of the faults geometry, the two main findings of the thorough study of Hill et al. (2015) were: (1) the main moment release was on young WNW trending right-lateral faults, contrary to previous assumptions that the reactivated NNE trending fracture zone played a primary role in the rupture process; (2) these faults ruptured deep down in the upper mantle with high stress drops (>20 MPa).

Our rupture solution agrees in general with the one of Hill et al. (2015). As should be expected, the seismic moment magnitude release on the fault planes is nearly identical to the Hill et al. (2015) results when considering GPS only solution. For plane I their estimate is M_w8.2, our solution for GPS data only, give 8.28, plane II – M_w8.1 (8.15), plane III – 8.5 (8.44) and for plane IV 8.2 (8.0). The values we obtain when solving for both GPS and GRACE are also close except for the plane IV, where the seismic moment magnitude decreases down to 7.34 compared to 8.2. According to the NEIC seismicity catalogue, the maximum magnitude of seismic events in the area of planes I-III in the period 01.01.2012 – 30.06.2012 was 8.6, whereas in the vicinity of plane IV it was only 6.2 (shown by small red circle on figures 4 and 5). Hence our result seems to better agree with seismological data. We also recall that the rupture model of Zang et al. (2012) does not contain this fault plane. The small estimated displacements on plane IV (30 cm) simply results from the fact that the fault-plane in our model is very large. Indeed, following (Hill et al., 2015) we assigned an along strike size of plane IV of 232 km, and along dip size as 44 km. However, it is well known that the size of a rupture surface for an earthquake of magnitude 6.2 is much smaller (e.g. Wells and Coppersmith, 1994).

In our joint GPS and GRACE solution, the seismic moment release on plane I is $2.44 \cdot 10^{21}$ $N{\cdot}m$, $2.65 \cdot 10^{21}$ $N{\cdot}m$ on plane II and $3.22 \cdot 10^{21}$ $N{\cdot}m$ on plane III. Therefore, as in Hill et al. (2015) we conclude that the main seismic moment release occurred on the WNW trending plane III. In our solution the seismic moment release on the NNE trending plane I is 2.4 times smaller than the total release at planes II and III. In Hill et al. (2015) solution, this ratio is larger: 3.7.

Different data including seismic profiles, magnetic anomalies and satellite gravity show that the NNE trending system plays important role in the regional geodynamics (Jacob et al., 2014 and references herein). Numerous structures seen at the sea-bottom and on seismic profiles have been presumably formed in result of strike-slip faulting. They extend to thousands of kilometres approximately in NS direction across the Wharton basin and further to the north in the Bengal Fan (Deplus et al., 1998; Franke et al., 2008, Matthews et al., 2011; Carton et al., 2014). Therefore, the higher energy release on plane I in our solution better suits the regional geodynamics. In our model strike of planes I and IV is 12^0 when strike of planes II and III is 108^0. To produce right lateral strike-slip at WNW faults and left lateral strike-slip at NNE faults simultaneously, the regional compressional stress should be directed NNW, somewhere in the middle between azimuth 12^0 and 288^0, i.e. close to 330^0. According to Singh et al. (2017) the principal compressional stress in the Wharton basin is oriented at 335°.

In their study, Hill et al. (2015) mention that their inversion is not able to resolve the depth to which coseismic rupture penetrated. Unfortunately, inclusion of satellite gravity data does not really help. McKenzie et al. (2005) and later Jackson et al. (2008) and Géli and Sclater (2008) suggested that the depth of the well constrained earthquake centroids is limited by the 600°C isotherm. Depth to the 600°C isotherm depends on the age of the lithosphere and thickness of sediments if no thermal rejuvenation occurred. Hill et al. (2015) estimated the depth to the 600°C isotherm in the epicentral area to be at about 30 km based on a diffusion model (Stein and Stein, 1992) and plate ages from Müller et al. (1997). Both half-space cooling model and plate-cooling model predict the depth of the 600° isotherm for a 50-60 my age lithosphere to be in the interval 33-38 km (e.g. Aderhold and Abercrombie, 2016, Fig.2). The thickness of sediments in the study area is 3-4 km (Carton et al., 2014). Sedimentary wedge slows down the cooling and uplifts the 600^0 isotherm but it also causes additional isostatic subsidence moving this isotherm down. Mikhailov & Timoshkina (1993) and Mikhailov et al. (2007) investigated the half-space cooling model taking into account sedimentation and latent heat of basalt crystallization at the lithosphere – asthenosphere interface. Using this solution and assuming a rate of sedimentation of 3-4 km per 50-60 my, the depth of the 600°C isotherm should be shifted down by ~ 4 km to a depth of about 40 km. Considering the results of waveform inversion and the estimation of centroid depths ranging from 30 to 45 km (Duputel et al., 2012), one may therefore conclude that the rupture penetrated slightly below the 600°C isotherm and probably some alternative mechanism to the frictional slip such as the thermal runaway mechanism may have to be considered (e.g., McGuire and Beroza, 2012).

5 Postseismic viscoelastic relaxation

Finally, we investigate the postseismic relaxation within the three years following the earthquakes. The GPS sites of the Sumatran GPS Array (SuGAr) registered coseismic and postseismic displacements. Postseismic ones appear to be as large as one fourth of the coseismic ones. GRACE time series also show some postseismic signal. Large-scale postseismic processes consist in creep (afterslip) and/or viscoelastic relaxation. As shown by Panet et al. (2010), the observed postseismic crustal displacements and gravity signals after the December 2004 great Andaman Sumatra earthquake are well explained by a viscoelastic relaxation model to which some afterslip on the downdip continuation of the ruptured surface is added. In this model, the asthenosphere (between 60 and 220 km depth) has a Burgers body rheology with transient and steady state viscosities equal to $4*10^{17}\ Pa \cdot s$ and $8*10^{18}\ Pa \cdot s$, respectively, and the mantle below depth 220 km has a Maxwell rheology with viscosity $8*10^{18}\ Pa \cdot s$ for the upper mantle and $8*10^{20}\ Pa \cdot s$ for the lower mantle. In addition, Mikhailov et al. (2013) showed how post-seismic stress initiated a gradual (∼1 m) slip localized at ∼100-km downdip extension of the coseismic rupture by modelling the seismic cycle in the area of Sumatra-2004 using a damage rheology.

Some authors explained the recorded postseismic surface displacements and satellite gravity signal after large events assuming only a viscoelastic relaxation with a low viscosity in the asthenosphere. For example, to fit GPS data in the area of the Simushir 2006-2007 earthquakes on the Kuril subduction zone, a Maxwell rheology with a viscosity as low as $2*10^{17}\ Pa \cdot s$ was suggested by Kogan et al. (2013). To fit CSR N=40 postseismic gravity signal in the same area Han et al. (2016) used a Maxwell rheology with a viscosity of $10^{18}\ Pa \cdot s$ for the asthenosphere. Using high-resolution GRACE models and GPS data we previously showed (Mikhailov et al., 2018) that at high resolution the synthetic gravity signal calculated assuming a low-viscosity Maxwell rheology does not fit the signal extracted from CSR N=96 GRACE models. On the other hand, the postseismic gravity signal could be well explained by postseismic creep in a wide zone around the coseismic rupture area, including a deeper continuation.

In the Wharton basin, postseismic processes seem to be much weaker. We estimated the postseismic displacement field and gravity signal for this area using our preferred fault plane model (26 elements) obtained by the joint inversion of GPS and gravity data (Fig. 5) and the VISCO1D software of F. Pollitz. The spherically symmetric layered Earth model used in this calculation is based on PREM (Dziewonski and Anderson, 1981) with a 60 km thick elastic lithosphere and a 160 km thick asthenosphere for which the viscosity is considered as an adjustable parameter. The postseismic viscoelastic relaxation produces displacements at GPS sites in the same direction as the coseismic ones. The computed postseismic gravity signal has the same pattern as the coseismic one. The amplitude of the postseismic gravity signal as well as the amplitude of the postseismic displacements strongly depends on the viscosity of the asthenosphere. Figure 6 shows that we fit the observed data assuming a Maxwell rheology with a viscosity of $10^{19}\ Pa \cdot s$. For a lower viscosity of $10^{18}\ Pa \cdot s$ the amplitudes of synthetic signals are one order of magnitude larger than the observed ones, whereas for a viscosity of $10^{20}\ Pa \cdot s$, the synthetic displacements at GPS sites are close to zero. Hence we conclude that in the region of the Wharton diffuse plate boundary, the GPS and GRACE gravity post seismic signals are well explained assuming the commonly used value for the asthenospheric viscosity of 10^{19} $Pa \cdot s$. Taking into account that a part of the observed data could be also due to some postseismic creep, this viscosity value is thus a lower estimate.

Figure 5

6. Summary

The main results of our study are as follows:

- We fitted both GPS and high resolution GRACE gravity data using the geometry of the faults system suggested by Hill et al., (2015) for the 2012 Wharton earthquakes. Our solution shows that even if the main displacements occurred on WNW trending faults, comparable displacements occurred also on a NNE trending one. Hence deformation in this diffuse plate boundary area appears to be accommodated along both orthogonal fault-systems. Our model also shows that the displacements on the faults close to the Ninety East Ridge were small.
- We suggest to use the most detailed gravity models available for the analysis of earthquake induced gravity signals.
- To invert with constraints on the rake angle, we suggest a new regularization which allows keeping the problem linear. This method yields a rather uniform displacement field on the fault planes, without asperities. This does not mean that asperities do not exist, but that GRACE gravity models with N=96 as well as displacements at GPS sites situated far from the epicentre are not sensitive enough to resolve local variations of displacement fields on the fault planes.
- We successfully explain the postseismic displacements at GPS sites and the postseismic gravity signal by viscoelastic relaxation with a commonly used asthenospheric Maxwell viscosity of $10^{19}\ Pa \cdot s$. Taking into account the limited postseismic aftershock activity we conclude that the postseismic slip in the area of the 2012 Wharton earthquakes was limited, contrary to what is often observed after large subduction event. Nevertheless, because a part of the observed signal could be attributed to afterslip, the obtained viscosity value should be considered as a lower limit of the asthenospheric viscosity below the Wharton basin.

7. Acknowledgements

We much appreciate the help of F. Pollitz (USGS) who shared his knowledge and software for coseismic and postseismic modelling. We thank K. Chanard for her comments on an early version of our manuscript. We thank SuGAr, CSR and GRGS teams who generously shared their data. We appreciate comments of three anonymous reviewers which allowed to largely improve the manuscript.

VM thanks Université Paris-Diderot for financial support during his stay in Paris. Development of methods of GRACE time-series analysis and regularization was supported by the Megagrant from the Ministry of Science and Education of the Russian Federation under project no. 14.W03.31.0033 “Geophysical studies, monitoring, and forecasting the development of catastrophic geodynamical processes in the Far East of the Russian Federation”. Our study was also supported by CNES through Tosca committee. Work on data analysis of VM and ET was supported by State task of IPE RAS. This study is a result of the cooperation between IPE Moscow and IPGP and is IPGP contribution #

References

Abercrombie, R. E., Antolik, M. & Ekström G. (2003). The June 2000 Mw 7.9 earthquakes south of Sumatra: Deformation in the India–Australia Plate. *Journal of Geophysical Research*, 108 (B1). doi:10.1029/2001JB000674

Aderhold, K., & Abercrombie, R. E. (2016). Seismotectonics of a diffuse plate boundary: Observations off the Sumatra-Andaman trench. *Journal of Geophysical Research: Solid Earth*, 121, 3462–3478. doi:10.1002/2015JB012721

Basuyau, C., M. Diament, C. Tiberi, G. Hetényi, J. Vergne, and A. Peyrefitte (2013), Joint inversion of teleseismic and GOCE gravity data: Application to the Himalayas *Geophys. J. Int.*, 193(1), 149 - 163. doi: 10.1093/ggi/ggs110

Boettcher, M. S., Hirth, G., & Evan B. (2007). Olivine friction at the base of oceanic seismogenic zones. *Journal of Geophysical Research*, 112, B01205. doi:10.1029/2006JB004301

Bull, J. M., & Scrutton, R. A. (1990). Fault reactivation in the central Indian Ocean and the rheology of oceanic lithosphere. *Nature*, 344 (# 6269), 855.

Burov E. (2011). Rheology and strength of the lithosphere. *Marin Petroleum Geology*, 28, 1402-1443. doi:10.1016/j.marpetgeo.2011.05.008

Carton, H., Singh, S. C., Hananto, N. D., Martin, J., Djajadihardja, Y. S., Udrekh, Franke, D., & Gaedicke C. (2014). Deep seismic reflection images of the Wharton Basin oceanic crust and uppermost mantle offshore Northern Sumatra: Relation with active and past deformation. *Journal of Geophysical Research: Solid Earth*, 119, 32-51. doi:10.1002/2013JB010291

Dai, Ch., Shum, C.K., Guo, J., Shang, K., Tapley, B., Wang, R. (2016). Improved source parameter constraints for five undersea earthquakes from north component of GRACE gravity and gravity gradient change measurements. *Earth and Planetary Science Letters*, 443, 118–128. doi.org/10.1016/j.epsl.2016.03.025

DeMets, C., Gordon, R. G., & Argus, D. F. (2010). Geologically current plate motions. *Geophysical Journal International*, 181(1), 1-80. doi: 10.1111/j.1365-246X.2009.04491.x

Deplus, C., Diament, M., Hébert, H., Bertrand, G., Dominguez, S., Dubois, J., Malod, J., Patriat, P., Pontoise, B., & Sibilla, J.-J. (1998). Direct evidence of active deformation in the eastern Indian oceanic plate. *Geology*, 26, 131–134.

Duputel, Z., Kanamori, H., Tsai, V. C., Rivera, L., Meng, L., Ampuero, J.-P., & Stock J. M. (2012). The 2012 Sumatra great earthquake sequence. *Earth and Planetary Science Letters*, 351-352, 247–257.

Dziewonski, A.M., & Anderson, D.L. (1981). Preliminary Reference Earth Model (PREM). *Physics of the Earth and Planetary Interiors*, 25, 297-356.

Geersen J., Bull J. M., McNeill, L. C., Henstock, T. J., Gaedicke, C., Chamot-Rooke, N., Delescluse M. (2015). Pervasive deformation of an oceanic plate and relationship to large> Mw 8 intraplate earthquakes: The northern Wharton Basin, Indian Ocean. *Geology*, 43(4), 359-362. doi.org/10.1130/G36446.1

Géli L., & Sclater J. (2008). On the depth of oceanic earthquakes: Brief comments on "The thermal structure of oceanic and continental lithosphere", by McKenzie, D., Jackson, J. and Priestley, K., Earth and Planetary Science Letters, [2005], 233, p. 337–349. *Earth and Planetary Science Letters*, 3 (265), 766-772. doi:10.1016/j.epsl.2007.08.029

Gordon, R.G., Argus, D.F. & Royer, J.-Y. (2008). Space geodetic test of kinematic models for the Indo-Australian composite plate, Geology, 36, 827–830, doi:10.1130/G25089A.1.

Han, S.-C., Sauber, J., & Pollitz F. (2015). Coseismic compression/dilatation and viscoelastic uplift/subsidence following the 2012 Indian Ocean earthquakes quantified from satellite gravity observations. *Geophysical. Research. Letters*, 42, 3764–3722. doi:10.1002/2015GL063819.

Han S., Sauber J., & Pollitz F. (2016). Postseismic gravity change after the 2006-2007 great earthquake doublet and constraints on the asthenosphere structure in the central Kuril Island. *Geophysical Research Letters,* 43(), 3169-3177. doi: 10.1002/2016GL068167

Hill E. M., Yue, H., Barbot, S., Lay, T., Tapponnier, P., Hermawan, I., Hubbard, J., Banerjee, P., Feng, L., Natawidjaja, D., Sieh K. (2015). The 2012 Mw8.6 Wharton Basin sequence: A cascade of great earthquakes generated by near-orthogonal, young, oceanic mantle faults, *Journal of Geophysical Research. Solid Earth*, 120, 3723–3747. doi:10.1002/2014JB011703

Ishii, M., Kiser, E., & Geist, E. L. (2013). Mw 8.6 Sumatran earthquake of 11 April 2012: Rare seaward expression of oblique subduction, *Geology*, 41(3), 319–322. doi:10.1130/G33783.1.

Jackson, J., McKenzie D., Priestley K., Emmerson B. (2008). New views on the structure and rheology of the lithosphere. Journal of Geological Society, 165, 453–465.

Jacob J., Dyment J., Yatheesh V. (2014). Revisiting the structure, age, and evolution of the Wharton Basin to better understand subduction under Indonesia. *Journal of Geophysical Research: Solid Earth*, 119 (1), 169-190. doi:10.1002/2013JB010285

Kogan M.G., Vasilenko, N.F., Frolov, D.I., Frymueller J.T. (2013). Rapid postseismic relaxation after the great 2006–2007 Kuril earthquakes from GPS observations in 2007–2011. *Journal of Geophysical Research: Solid Earth,* 118, 3691-3706. DOI:10.1002/jgrb.50245.

Kusche J. (2007), Approximate decorrelation and non-isotropic smoothing of time-variable GRACE-type gravity field models. *Journal of Geodesy*, 81(11), p. 733-749.

Kusche, J., Schmidt, R. , Petrovic, S., Rietbroek, R. (2009). Decorrelated GRACE time-variable gravity solutions by GFZ, and their validation using a hydrological model. *Journal of geodesy*, 83(10), 903–913.

Lemoine, J. M., Bruinsma, S., Gégout, P., Biancale, R., Bourgogne, S. (2013). Release 3 of the GRACE gravity solutions from CNES/GRGS. In: *EGU General Assembly Conference Abstracts*, 15.

Liu, C. S., J. R. Curray, and J. M. McDonald (1983), New constraints on the tectonic evolution of eastern Indian Ocean, *Earth Planet. Sci. Lett.*, 65, 331–342.

Lorito, S., Piatanesi, A., Cannelli, V., Romano, F., Melini, D. (2010). Kinematics and source zone properties of the 2004 Sumatra-Andaman earthquake and tsunami: Nonlinear joint inversion of tide gauge, satellite altimetry, and GPS data. *Journal of Geophysical Research: Solid Earth*, 115, B02304. doi:10.1029/2008JB005974

McGuire, J. J., & Beroza G. C. (2012). A rogue earthquake off Sumatra. *Science,* 336, 1118–1119.

McKenzie, D., Jackson, J., & Priestley K. (2005). Thermal structure of oceanic and continental lithosphere, *Earth and Planetary Science Letters*, 233, 337–349.

Meng, L., Ampuero, J. P., Stock, J., Duputel, Z., Luo, Y., & Tsai, V. C. (2012). Earthquake in a maze: Compressional rupture branching during the 2012 Mw 8.6 Sumatra earthquake. *Science*, 337(6095), 724-726. DOI: 10.1126/science.1224030

Mikhailov, V.O., Timoshkina, E.P. (1993). Analysis of data on the Nansen cordillera, assuming a thermal model of an oceanic lithosphere. *Proceedings (Doklady) of Russian Academy of Sciences*, 331, 497-499.

Mikhailov, V., Tikhotsky, S., Diament, M., Panet, I., & Ballu, V. (2004). Can tectonic processes be recovered from new gravity satellite data? *Earth and Planetary Science Letters*, 228(3-4), 281-297. doi:10.1016/j.epsl.2004.09.035

Mikhailov V., Lyakhovsky V., Panet, I., van Dinther, Y., Diament, M., Gerya, T., deViron, O., Timoshkina, E. (2013). Numerical modelling of post-seismic rupture propagation after the Sumatra 26.12.2004 earthquake constrained by GRACE gravity data. *Geophysical Journal International*, 94 (2), 640-650. doi: 10.1093/gji/ggt

Mikhailov V., Parsons, T., Simpson, R. W., Timoshkina, E., Williams, C. (2007). An explanation for deep earthquakes under the Sacramento Delta, California, in terms of deep structure and thermal history. *(Izvestiya) Physics of the Solid Earth*, 43 (1), 75-90.

Mikhailov V. O., Diament, M., Timoshkina, E. P., Khairetdinov, S. A. (2018). Assessment of the Relative Roles of Viscoelastic Relaxation and Postseismic Creep in the Area of the Simushir Earthquake of November 15, 2006, Using Space Geodesy and Gravimetry. *Moscow University Physics Bulletin*, 73 (5), 551–557. DOI: 10.3103/S0027134918050120

Mikhailov V. O., Timoshkina E. P. (2019). Geodynamic Modeling of the Process of the Formation and Evolution of Lithospheric Structures: the Experience of Schmidt Institute of Physics of the Earth, RAS. Izvestiya, Physics of the Solid Earth, 55(1), pp. 102–110. DOI: 10.1134/S1069351319010063

Müller, R. D., Roest, W. R., Royer, J.-Y., Gahagan, L. M., & Sclater, J. G. (1997). Digital isochrons of the world's ocean floor, *Journal of Geophysical Research: Solid Earth*, 102(B2), 3211–3214.

Panet, I., Pollitz, F., Mikhailov, V., Diament, M., Banerjee, P., & Grijalva, K. (2010). Upper mantle rheology from GRACE and GPS post-seismic deformations after the 2004 Sumatra-Andaman earthquake. *Geochemistry, Geophysics, Geosystems (G3)*, 11 (6), Q06008. doi:10.1029/2009GC002905.

Patriat, P., and J. Achache (1984), India-Eurasia collision chronology has implications for crustal shortening and driving mechanism of plates, *Nature*, 311, 615–621.

Petroy D.E. et Wiens D. A. (1989). Historical seismicity and implications for diffuse plate convergence in the northeast Indian Ocean. *Journal of Geophysical Research: Solid Earth*, 94 (B9), 12301-12319. DOI:10.1029/JB094iB09p12301

Pollitz, F.F. (1996), Coseismic deformation from earthquake faulting on a layered spherical Earth. *Geophysical Journal International*, 125, 1-14. doi.org/10.1111/j.1365-246X.1996.tb06530.x

Qin Y., & Singh S. C., (2015). Seismic evidence of a two-layer lithospheric deformation in the Indian Ocean. *Nature communications*, 6, 8298. DOI: 10.1038/ncomms9298

Rajendran K., Andrade, V., Rajendran, C. P. (2011). The June 2010 Nicobar earthquake: Fault reactivation on the subducting oceanic plate. *Bulletin of the Seismological Society of America*, 101 (5), 2568-2577. doi:10.1785/0120110002

Satriano, C., Kiraly, E., Bernard, P., & Vilotte, J.-P. (2012), The 2012 Mw 8.6 Sumatra earthquake: Evidence of westward sequential seismic ruptures associated to the reactivation of a N-S ocean fabric. *Geophysical Research Letters*, 39, L15302, doi:10.1029/2012GL052387.

Singh S. C., Hananto, N., Qin, Y., Leclerc, F., Avianto, P., Tapponnier, P.E., Carton, H., Wei, S., Nugroho, A.B., Gemilang, W.A., Sieh, K., Barbot, S. (2017). The discovery of a conjugate system of faults in the Wharton Basin intraplate deformation zone. *Science Advances*, 3(1), e1601689. DOI: 10.1126/sciadv.1601689

Stein, C. A., & Stein, S. (1992). A model for the global variation in oceanic depth and heat flow with lithospheric age. *Nature*, 359, 123–129.

Tiberi, C., M. Diament, J. Déverchère, C. Petit-Mariani, V. Mikhailov, S. Tikhotsky, and U. Achauer (2003), Deep structure of the Baikal rift zone revealed by joint inversion of gravity and seismology, *J. Geophys. Res.*, 108(B2), 2109,doi:2110.1029/2002JB001880.

Yadav R.K., Kundu B., Gahalaut K., Catherine J., Gahalaut V.K., Ambikapthy A., Naidu M. S. (2013). Coseismic offsets due to the 11 April 2012 Indian Ocean earthquakes (Mw 8.6 and 8.2) derived from GPS measurements. *Geophysical Research Letters*, 40, 3389–3393, doi:10.1002/grl.50601.

Yue, H., Lay, T., & Koper, K. D. (2012). En échelon and orthogonal fault ruptures of the 11 April 2012 great intraplate earthquakes. *Nature*, 490, 245–249, doi:10.1038/nature11492.

Wells D.L., Coppersmith K.J., (1994) New empirical relationships among magnitude, rupture length, rupture width, rupture area, and surface displacement. *Bulletin of the Seismological Society of America*. 84 (4). 974–1002.

Wei, S., Helmberger, D. , & Avouac, J.-P. (2013). Modeling the 2012 Wharton basin earthquakes off-Sumatra: Complete lithospheric failure. *Journal of Geophysical Research: Solid Earth*, 118, 3592–3609, doi:10.1002/jgrb.50267.

Zhang, H., Chen, J., & Ge, Z. (2012). Multi-fault rupture and successive triggering during the 2012 Mw 8.6 Sumatra offshore earthquake. *Geophysical Research Letters*, 39, L22305, doi:10.1029/2012GL053805.

Figure captions

Fig.1 Location of the M_w8.6 strike-slip seismic event of 11 April 2012 in the Wharton Basin. Green and yellow stars mark epicenters of the main aftershock M_w8.2, which occurred 2 hours later and the main foreshock M_w7.6 of 10 January 2012. Colored dots show position and depth of seismic events from the USGS NEIC catalogue for the period 10 January-28 December 2012. Solid black lines show the rupture model of Hill et al. (2015). The topography and bathymetry are from ETOPO1 (https://maps.ngdc.noaa.gov/).

Figure 2. Comparison of the gravity signal (in μGals) for the April 2012 Wharton earthquakes using the GRACE models of CSR and GRGS for the period 01/2008 - 06/2014 with different resolution. Dashed-dot line shows Sumatra trench, solid curve marks the shoreline. A – coseismic jump calculated as the difference between average values before and after the earthquake (eq. 4) using not filtered CSR models truncated at N=40. Crosses show the locations of extrema from Han et al. (2015). B –same as A, but using CSR N=96 models filtered by DDK5 and applying (eq. 4). C –same as B, but based on GRGS N=80 models. D – coseismic jump estimates as the difference of two trends (2) with annual and semi-annual components using CSR N=96 models. E – coseismic plus postseismic signal calculated using eq. (3) and CSR N=96 models also with annual and semi-annual components.

Fig. 3 Time-series (μGals) in the vicinity of (95E, -3S). Note the higher noise level in the un-filtered CSR N=40 model.

Fig.4. Gravity anomaly in μGals calculated using the fault planes model geometry of Hill et al. (2015) in result of inversion of GPS data only. Black lines – projection of vertical fault planes to the Earth surface. Green and black arrows show synthetic and real GPS coseismic displacements. Coloured maps on plot A and B are the observed coseismic gravity signals from Fig.2B and A. Dotted isolines show the synthetic signals: (a) truncated at N=80 for the more detailed model, (b) truncated at N=40 signal for the simple model. Crosses on the right plot show position of extrema in Han et al. (2015). Red circles mark the main seismic events (size proportional to magnitude). Small circle close to plane IV shows the strongest event M_w6.2 which occurred in vicinity of this plane.

Fig.5. Comparison of real (Fig. 2b) and synthetic gravity signals and GPS displacements for the fault plane model based on Hill et al. (2015) geometry and joint inversion of GPS and CSR N=96 data with regularization (6).

Fig. 6

a - Postseismic gravity signal (in µGal, N=80 SH) during two years after the April 2012 event in result of viscoelastic relaxation calculated using F. Pollitz code VISCO1D and our model based on GPS and GRACE data. For notations see Fig 4,5.

b – Comparison of coseismic plus postseismic signals. Coloured scale shows real data (Fig.2E), isolines – synthetic coseismic (Fig.2 D) plus postseismic (Fig.6a) signals.

c – Solid curves show amplitude of total (black), easting (red) and northing (blue) displacements at two GPS sites of the Sumatran GPS Array (SuGAr). Symbols of the same colour show modelled displacements assuming an asthenospheric viscosity of 10^{19} $Pa \cdot s$*. Horizontal axis shows time, vertical axis is displacements (meters).*

Table 1 Solutions for different number of elements in planes I-IV using GPS only (lines 1, 2) and GPS+gravity (line 3). GPS misfit is maximum value of difference between real and synthetic absolute displacements at GPS sites in %.

Highlights

- We fitted both GPS and high resolution GRACE gravity data using the geometry of the faults system suggested by Hill et al., (2015) for the 2012 Wharton earthquakes. To invert with constrains on the rake angle, we suggest a new regularization, which allows keeping the problem linear. This method yields a rather uniform displacement field on the fault planes, without asperities.
- Our solution shows that even if the main displacements occurred on WNW trending faults, comparable displacements occurred also on a NNE trending one. Hence, deformation in this diffuse plate boundary area appears to be accommodated along both orthogonal fault-systems.
- A viscoelastic relaxation with a commonly used asthenospheric Maxwell viscosity of $10^{19}\ Pa \cdot s$ successfully explains the postseismic displacements at GPS sites and the postseismic gravity signal. Because part of the observed signal could be attributed to afterslip, the obtained viscosity value should be considered as a lower limit of the asthenospheric viscosity below the Wharton basin.

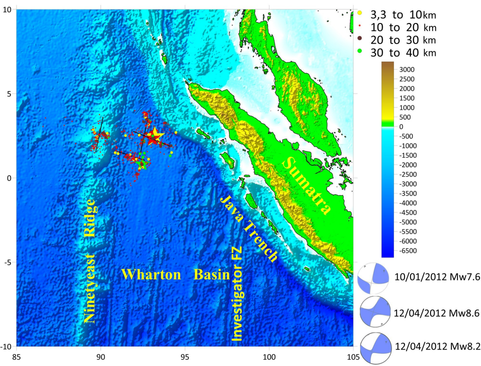

● 3,3 to 10km
● 10 to 20 km
● 20 to 30 km
● 30 to 40 km
3000
2500
2000
1500
1000
500
0
-500
-1000
-1500
-2000
-2500
-3000
-3500
-4000
-4500
-5000
-5500
-6000
-6500
Sumatra
Java Trench
Ninetyeast Ridge
Wharton Basin
Investigator FZ
10/01/2012 Mw7.6
12/04/2012 Mw8.6
12/04/2012 Mw8.2
10
5
0
-5
-10
85
90
95
100
105


A
B
C
D
E
10
8
6
4
2
0
-2
-4
-6
-8
82
84
86
88
90
92
94
96
98
9
7
5
3
-3
-5
-7
11
-9
-11
13
-9.5
3
-3
5
-5
7
-7

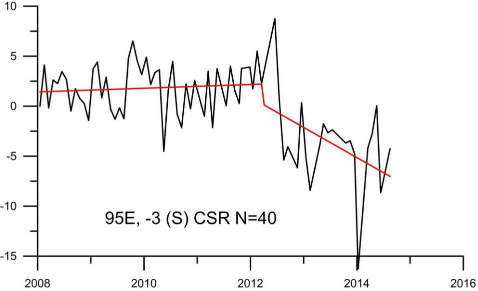
10
5
0
-5
-10
-15
95E, -3 (S) CSR N=40
2008
2010
2012
2014
2016

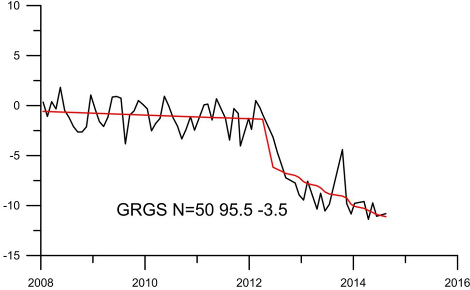
10
5
0
-5
-10
-15
GRGS N=50 95.5 -3.5
2008
2010
2012
2014
2016

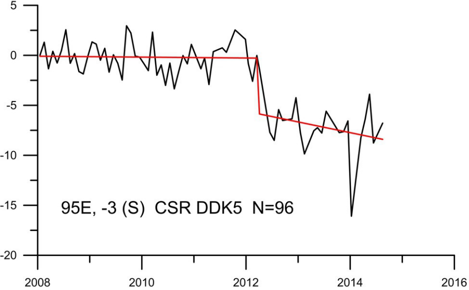
5
0
-5
-10
-15
-20
95E, -3 (S) CSR DDK5 N=96
2008
2010
2012
2014
2016

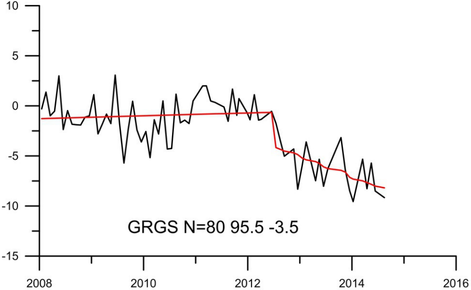
10
5
0
-5
-10
-15
GRGS N=80 95.5 -3.5
2008
2010
2012
2014
2016

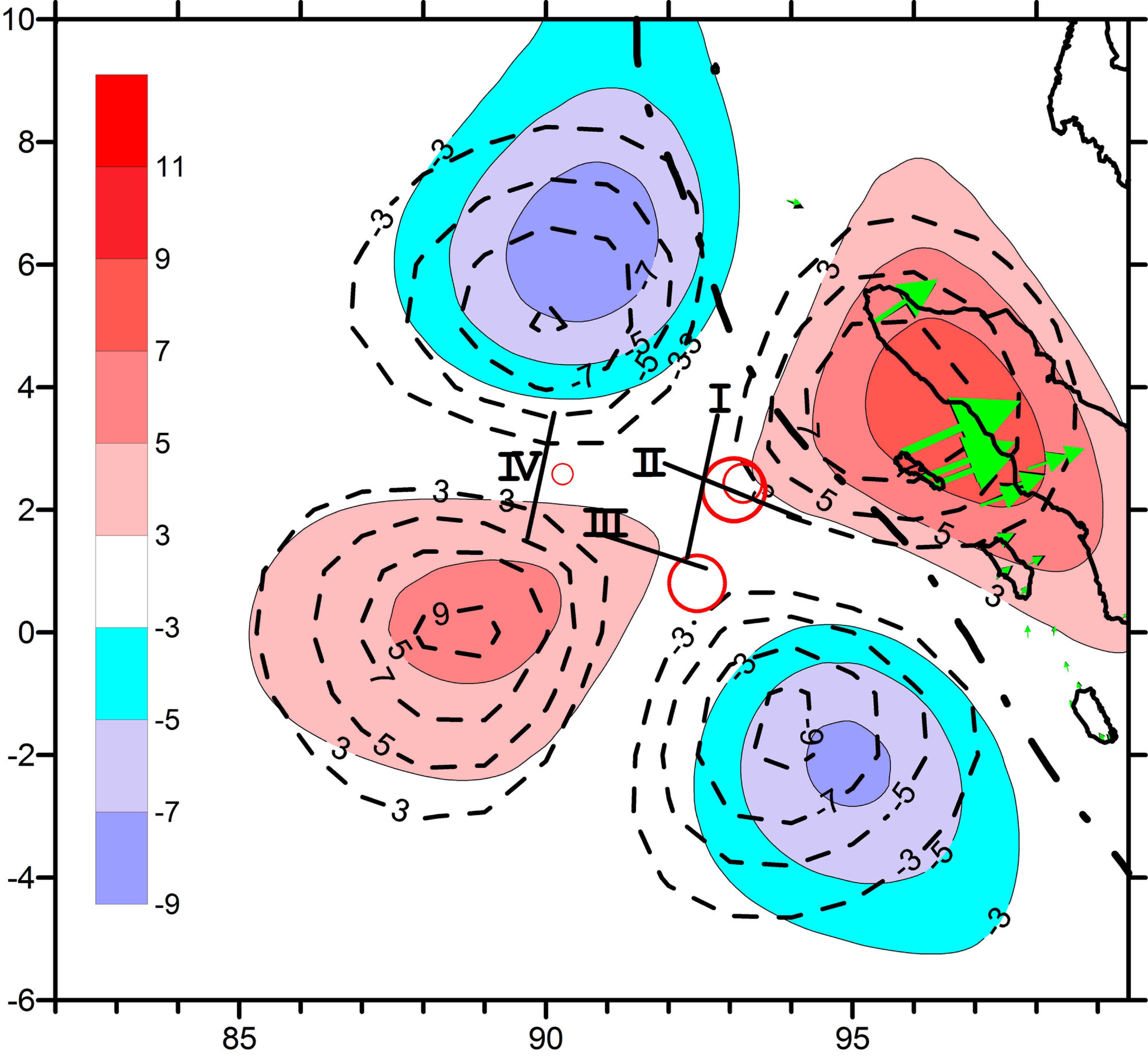
10
8
6
4
2
0
-2
-4
-6
85
90
95
11
9
7
5
3
-3
-5
-7
-9
I
II
III
IV

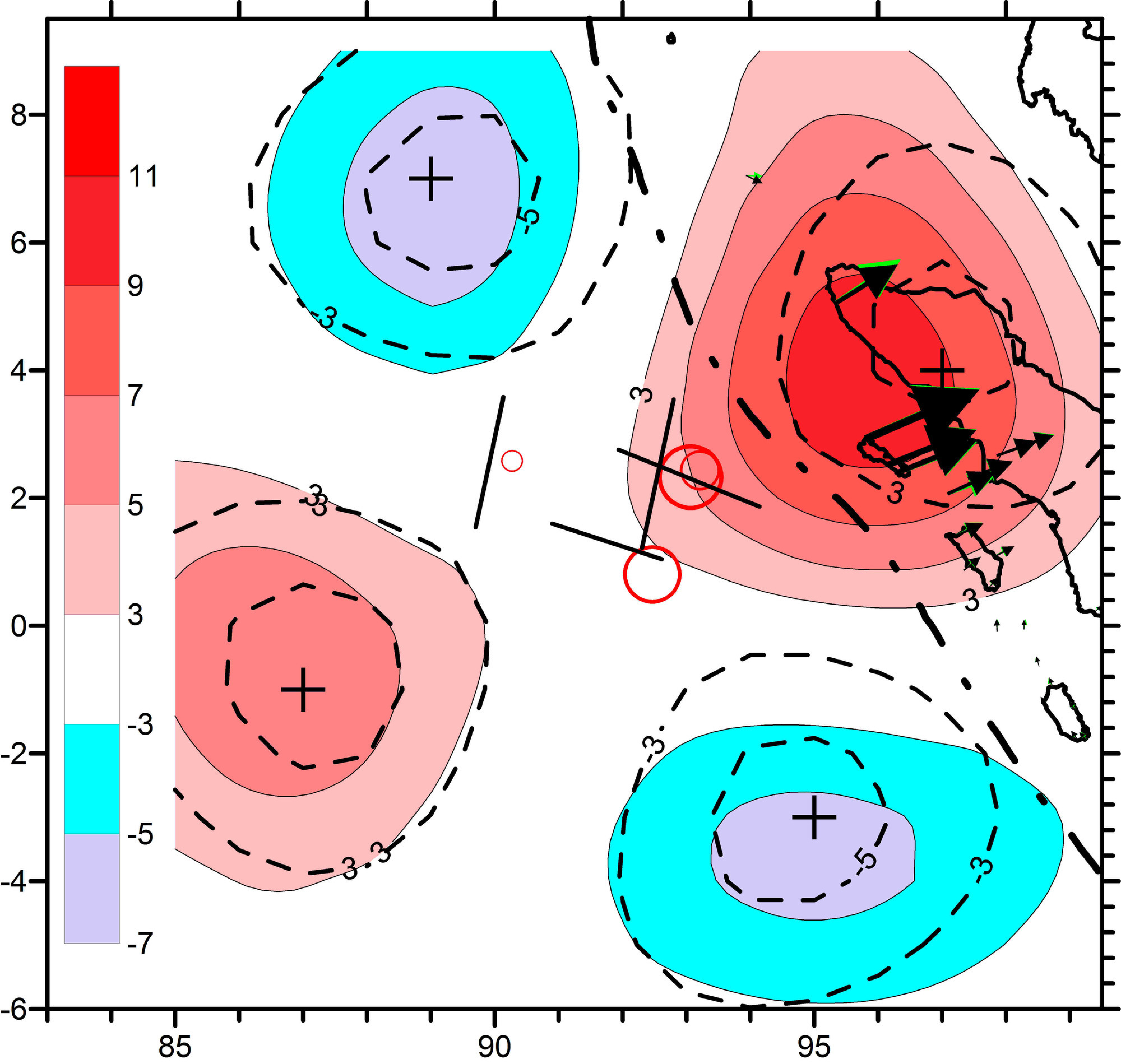

11
9
7
5
3
-3
-5
-7
8
6
4
2
0
-2
-4
-6
85
90
95
-5
-3
3
3
3
3
3
3
-3
-5
-3

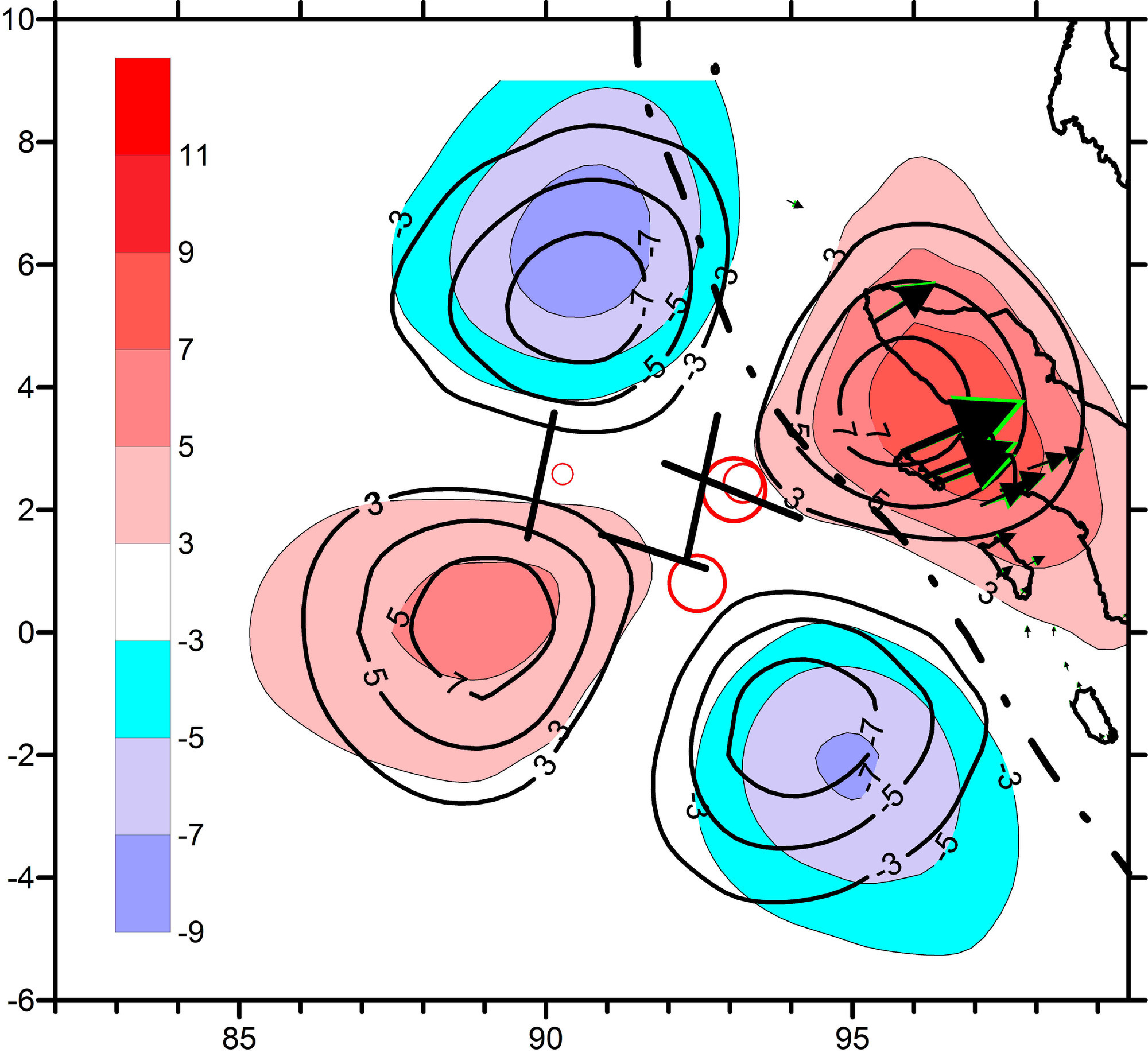
10
8
6
4
2
0
-2
-4
-6
85
90
95
11
9
7
5
3
-3
-5
-7
-9

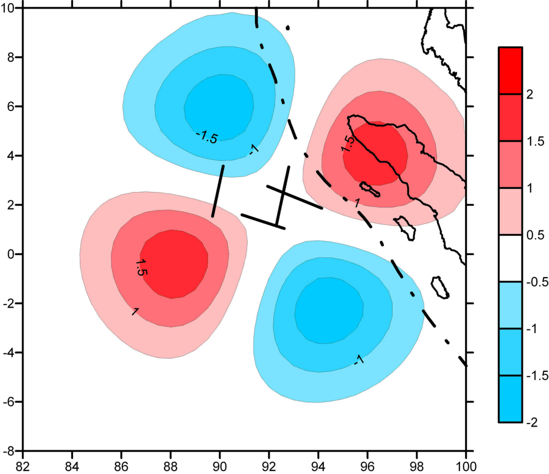
10
8
6
4
2
0
-2
-4
-6
-8
82
84
86
88
90
92
94
96
98
100
-1.5
-1
1.5
1
1.5
1
-1
2
1.5
1
0.5
-0.5
-1
-1.5
-2

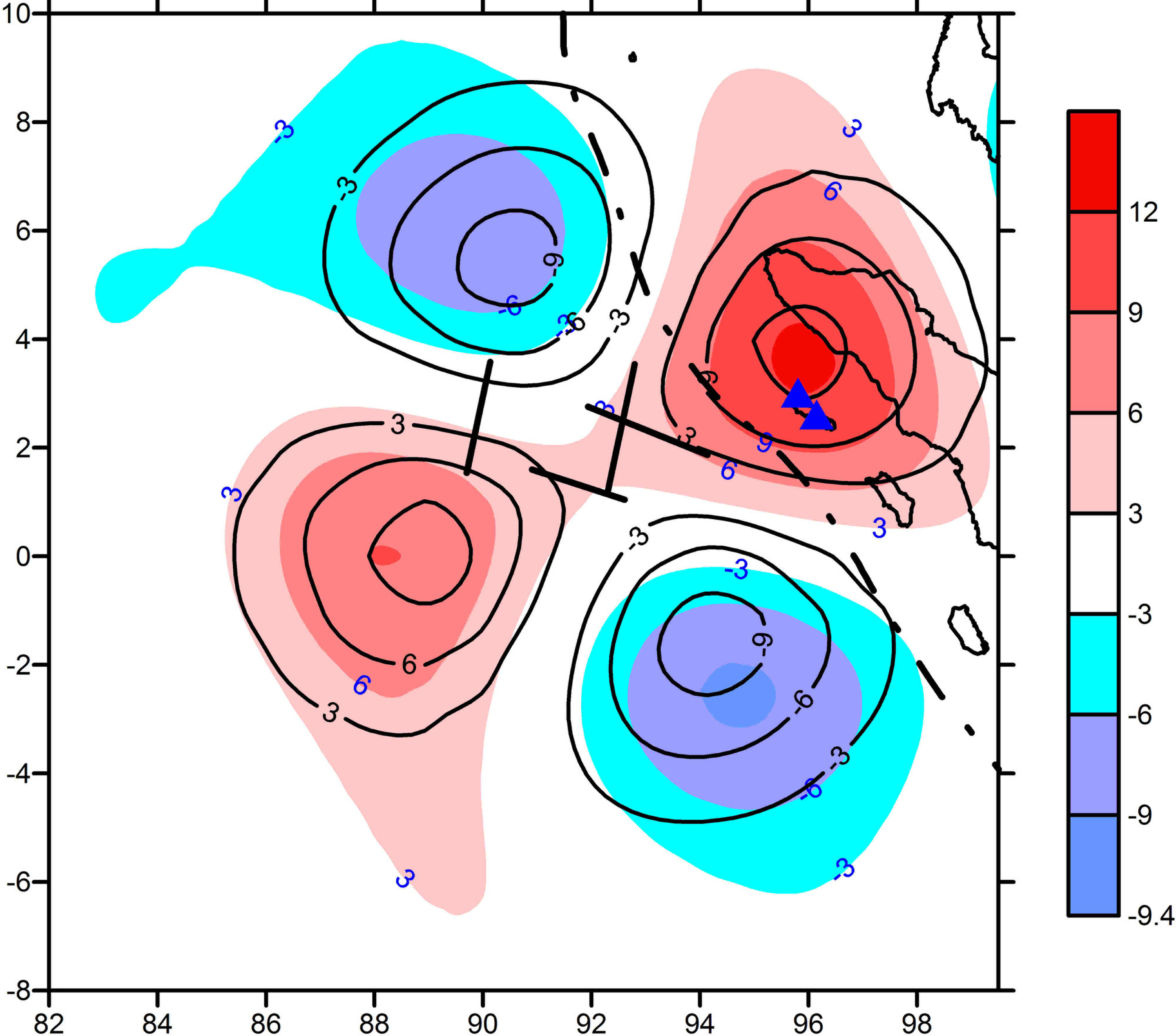
10
8
6
4
2
0
-2
-4
-6
-8
82
84
86
88
90
92
94
96
98
12
9
6
3
-3
-6
-9
-9.4
-3
-3
-9
-6
-6
-3
-3
3
6
9
6
3
3
3
3
6
0
6
6
3
3
-3
-3
-9
-6
-3
-6
-3

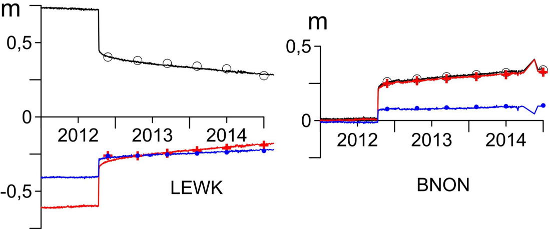
m
0,5
0
-0,5
2012
2013
2014
LEWK
m
0,5
0
2012
2013
2014
BNON

Table 1 Solutions for different number of elements in planes I-IV using GPS only (lines 1, 2) and GPS+gravity (line 3). GPS misfit is maximum value of difference between real and synthetic absolute displacements at GPS sites in %.

Number of elements	Dip slip (min, max) / Strike slip (min, max)				GPS misfit	V_z misfit
	plane I	plane II	plane III	plane IV	Δ module (%)	RMS (μGal)
10	(-.010;-0.10)/ (7.23-7.28)	(-0.17;-0.15)/ (4.77;4.79)	(0.04;0.04)/ (17.40-17.42)	(-0.05;-0.05)/ (3.55;3.55)	9.1	2.4
26	(-.005;-0.04)/ (7.24-7.28)	(-0.06;-0.09)/ (4.77;4.81)	(0.02;0.03)/ (17.34-17.41)	(-0.03;-0.03)/ (3.56;3.57)	9.2	1.9
26+V_z	(-0.06;0.06)/ (6.93;7.04)	(-0.40;-0.23)/ (7.56;7.64)	(-0.34;-0.18)/ (12.11;12.32)	(0.27;0.37)/ (0.26;0.30)	7.0	1.5